Variations in surface roughness of heterogeneous surfaces in the Nagqu area of the Tibetan Plateau

Maoshan Li[*1], Xiaoran Liu[2], Lei Shu[1], Shucheng Yin[1], Lingzhi Wang[1], Wei Fu[1],

Yaoming Ma [3], Yaoxian Yang[4], Fanglin Sun [4]

(1.School of Atmospheric Sciences/Plateau Atmosphere and Environment Key Laboratory of Sichuan Province/Joint Laboratory of Climate and Environment Change, Chengdu University of Information Technology, Chengdu 610225, Sichuan China;

2. Climate Center, Meteorological Bureau of Inner Mongolia Autonomous Region, Huhehot 010051, Inner Mongolia Autonomous Region, China)

3.Key Laboratory of Tibetan Environment Changes and Land Surface Processes, Institute of Tibetan Plateau Research, Chinese Academy of Sciences, CAS Center for Excellence in Tibetan Plateau Earth Sciences, Beijing, China;

3. Key Laboratory of Land Surface Process and Climate Change in Cold and Arid Regions, Chinese Academy of Sciences. Lanzhou, China)

Abstract: Temporal and spatial variations of the surface aerodynamic roughness lengths (Z_{0m}) in the Nagqu area of the northern Tibetan Plateau were analysed in 2008, 2010, and 2012 using MODIS satellite data and in-situ atmospheric turbulence observations. Surface aerodynamic roughness lengths were calculated from turbulent observations by a single height ultrasonic anemometer and retrieved by the Massman model. The results showed that Z_{0m} has an apparent characteristic of seasonal variation. From February to August, Z_{0m} increased as snow ablation and vegetation growth, and the maximum value reached 4-5 cm at the BJ site. From September to February, Z0m gradually decreased and reached its minimum values of about 1-2 cm. Snowfall in abnormal years was the main reason for the significantly lower Z0m compared with that in normal conditions. The underlying surface can be divided into four categories according to the different values of Z0m: snow and ice, sparse grassland, lush grassland, and town. Among them, lush

---

[*] Corresponding author

Dr. Maoshan Li

Chengdu University of Information Technology

24 Block 1, Xuefu Road, Chengdu 610225, Sichuan, China

E-mail: lims@cuit.edu.cn

27 grassland and sparse grassland accounted for 62.49% and 33.74%, and they have an annual

28 variation of Z_{0m} between 1-4 cm and 2-6 cm, respectively. The two methods were positively

29 correlated, and the retrieved values were lower than the measured results due to the heterogeneity

30 of the underlying surface. These results are substituted into Noah-MP to replace the original

31 parameter design numerical simulation experiment. After replacing the model surface roughness,

32 the sensible heat flux and latent heat flux were simulated with a better diurnal dynamics.

33 **Key words:** Northern Tibetan Plateau; Surface roughness; NDVI; MODIS

1 Introduction

36 Known as the "third pole" of Earth (Jane, 2008), the Tibetan Plateau (TP) has an average

37 altitude of over 4000 m and accounts for a quarter of China's territory. It is located in southwestern

38 China adjacent to the subtropical tropics in the south, and it reaches the mid-latitudes in the north,

39 making it the highest plateau in the world. Due to its special geographical location and

40 geomorphic characteristics, it plays an important role in the global climate system as well as the

41 formation, outbreak, duration and intensity of the Asian monsoon (Yang et al., 1998; Zhang et al.,

42 1998; Wu et al., 1999, 2004, 2005; Ye et al, 1998; Wu et al, 1998; Tao et al, 1998). Many studies

43 (Wu et al., 2013; Wang, 1999; Ma et al, 2002) have shown that the land-atmosphere interaction on

44 the TP plays an important role in the regional and global climate. Over the past 47 years, the

45 Tibetan Plateau has shown a significant warming trend and increased precipitation (Li et al., 2010).

46 The thermal effects of the Tibetan Plateau not only have an important impact on the Asian

47 monsoon and precipitation variability but also affect the atmospheric circulation and climate in

48 North America, Europe and the South Indian Ocean by inducing large-scale teleconnections

49 similar to the Asia-Pacific Oscillation (Zhou et al., 2009).

50 The various thermal and dynamic effects of the Tibetan Plateau on the atmosphere affect the

51 free atmosphere via the atmospheric boundary layer. Therefore, it is particularly important to

52 analyse the micrometeorological characteristics of the atmospheric boundary layer of the Tibetan

53 Plateau, especially the near-surface layer (Li et al., 2000). Affected by the unique underlying

54 surface conditions of the Tibetan Plateau, local heating shows interannual and interdecadal

55   variability (Zhou et al., 2009). Different underlying surfaces have differing diversities, complex

56   compositions and uneven distributions, which also makes the land surface that they constitute

57   diverse and has a certain degree of complexity. As the main input factor for atmospheric energy,

58   the surface greatly affects the various interactions between the ground and the atmosphere and

59   even plays a key role in local areas or specific times (Guan et al, 2009). The surface characteristic

60   parameters (dynamic roughness, thermodynamic roughness, etc.) play an important role in the

61   land surface process and are important factors in causing climate change (Jia et al., 2000). The

62   underlying surface of the Tibetan Plateau presents different degrees of fluctuation, which

63   introduces certain obstacles to understanding the land-atmosphere interaction of the Tibetan

64   Plateau. The fluctuating surface may alter the arrangement of roughness elements on the surface

65   and cause changes in surface roughness. Changes in roughness can also affect changes in the

66   characteristics of other surface turbulent transportation, which may also result in changes in

67   surface fluxes. Chen et al. (2015) presented a practical approach for determining the aerodynamic

68   roughness length at fine temporal and spatial resolutions over the landscape by combining remote

69   sensing and ground measurements. Surface roughness is an important parameter in land surface

70   models and climate models. Its size controls the exchange, transmission intensity and interactions

71   between the near surface airflow and the underlying surface to some extent (Liu et al., 2007;

72   Irannejad et al, 1998; Shao et al, 2000; Zhang et al., 2003). Zhou et al. (2012) demonstrated that

73   simulated sensible heat flux compared with measurement was significantly improved by using a

74   time-dependent Z0m parameter. Therefore, the primary objective of this study is to calculate the

75   surface roughness and its variation characteristics to further understand the land-atmosphere

76   interactions on the central Tibetan Plateau.

77   Through the study of surface roughness, it is beneficial to obtain the land surface

78   characteristics in the region, provide the ground truth value for model inputs, improve land surface

79   simulations in the Tibetan Plateau, and deepen the understanding of land-atmosphere interaction

80   processes. Simulation of surface fluxes has been made considerable progress in recent years,

81   especially in the improvement of parameterization schemes (Smirnova et al., 2016). Luo et al.

82   used the land surface model CoLM to conduct a single-point numerical simulation at the BJ

83   station and successfully simulated the energy exchange process in the Nagqu area (Luo et al.,

84   2009). Zhang et al. evaluated the surface physical process parameterization schemes of the Noah

85   LSM and Noah-MP models in the entire East Asia region and evaluated the simulation of the

86   surface heat flux of the Tibetan Plateau (Zhang et al., 2017). Xie et al. explored the simulation

87   effect of the land surface model CLM4.5 in the alpine meadow area of the Qinghai-Tibet Plateau

88   (Xie et al., 2017). Xu et al. studied the applicability of different parameterization schemes in the

89   WRF model when simulating boundary layer characteristics in the Nagqu area (Xu, et al., 2018).

90   Zhang, et al. Comparative analyses have been performed of the meteorological elements simulated

91   by different land surface process schemes in the WRF model in the Yellow River source region

92   (Zhang et al., 2019). However, the applicability of the model in the Tibetan Plateau needs further

93   study. The terrain of the Tibetan Plateau is complex, the underlying surface is very uneven, and the

94   area has high spatial heterogeneity. Because the condition of the underlying surface has a very

95   significant impact on the surface flux, obtaining information on the surface vegetation status of a

96   certain area is very helpful for analysing the spatial representation of the surface flux.

97   In this study, satellite data were obtained by MODerate-resolution Imaging

98   Spectroradiometer (MODIS) and the normalized difference vegetation index (NDVI) in the Nagqu

99   area was used to study the dynamic surface roughness length. Atmospheric turbulence observation

100 data in 2008, 2010, and 2012 and observation data from automatic weather stations were collected

101 at three observation stations. The measured values of the average wind speed and turbulent flux of

102 a single height ultrasonic anemometer were used to determine the surface dynamic roughness $Z0m$

103 (Chen et al., 1993). The time-scale dynamics of $Z0m$ and the results of different underlying

104 surfaces were analysed. Through a comparison of the calculation results to the observation data,

105 we studied whether the surface roughness values retrieved by satellites were reliable to provide

106 accurate surface characteristic parameters. Then we used the retrieved surface roughness to

107 replace the surface roughness in the original model for numerical simulation experiments, and

108 evaluated the model simulation results. These researches will be helpful for the study of

109 land-atmosphere interactions in the plateau area and improving the theoretical research of the

110 near-surface layer on the Tibetan Plateau. In the following section, we describe the case study area,

111   the MODIS remote sensing data, the ground observations, and the land cover map used to drive

112   the revised Massman model (Massman et al, 1997, 1999). In Section 3, we present the results and

113   then a validation based on flux measurements at Nagqu station. Finally, we provide some

114   concluding remarks on the variation characteristics of aerodynamic roughness lengths and

115   numerical simulation of the surface turbulent flux in the Nagqu area of the central Tibetan Plateau.

116

2 Study area, Data and methods

2.1 Study area and Data

119   The area selected in this study is a 200×200 km^2 area centred on the Nagqu Station of Plateau

120   Climate and Environment of the Northwest Institute of Ecology and Environmental Resources,

121   Chinese Academy of Sciences.

122   In this area, three meteorological observatory stations are located: North Pam (Portable

123   Automated Meso-net) Automatic Meteorological Observatory (NPAM), Nam Co Station for

124   Multisphere Observation and Research, Chinese Academy of Sciences (NAMC), and BJ station

125   (Figure 1). The underlying surface around the observation site is relatively flat on a small spatial

126   scale, and a certain undulation is observed at a large spatial scale. The data used included

127   observations from atmospheric turbulence and automatic meteorological stations.

128   The BJ station is located at coordinates 31.37°N, 91.90°E and has an altitude of 4509 m a.s.l.

129   The BJ observation site is located in the seasonal frozen soil area, and the vegetation is alpine

130   grassland. The site measurement equipment includes an ultrasonic anemometer (CAST3,

131   Campbell, Inc.), CO2/H2O infrared open path analyser (LI 7500), and an automatic

132   meteorological observation system (Ma et al., 2006). This study uses the BJ station data from

133   2008 and 2012. The NPAM station is located at 31°56'N, 91°43'E and has an altitude of

134   approximately 4700 m. The ground of the experimental field is flat, and the area is wide. The

135   ground is covered by a plateau meadow that grows 15 cm high in summer. The experimental

136   station observation equipment includes an ultrasonic wind thermometer and humidity probe

137   pulsator and includes data on temperature and humidity, air pressure, average wind speed, average

138   wind direction, surface radiative temperature, soil heat flux, soil moisture and temperature, and

139 radiation (Ma et al., 2006). The NAMC station is located at 30°46.44'N, 90°59.31'E and has an

140 altitude of 4730 m. It is located on the southeastern shore of NAMC Lake in Namuqin Township,

141 Dangxiong County, Tibet Autonomous Region. It is backed by the Nyainqentanglha Mountain

142 Range, and the underlying surface is an alpine meadow. This study uses NPAM station data for the

143 whole year of 2012 and NAMC station data for the whole year of 2010.

144 **Figure 1 about here**

145 **Table 1 about here**

146 The land cover data used in this study are GLC2009 (Arino et al, 2010) data from the Envisat

147 satellite in 2009, and the spatial resolution is 300 m. The classification standard is the land cover

148 classification system (LCCS), and it divides the global surface into 23 different types, with the

149 study area including 14 of these types. The actual situation in the selected area does not match the

150 data part of GLC2009 because of the lack of an underlying surface, such as farmland, in the

151 selected area. Therefore, according to the actual land cover types obtained by Chu (Chu, 2010),

152 the categories irrigated farmland, dry farmland, mixed farmland vegetation, mixed multivegetation

153 land, closed grassland and open grassland are replaced with 6 grasslands, shrub meadows,

154 mountain meadows, alpine grasslands, alpine meadows and sparse vegetation in the mountains.

155 Since the proportion of the underlying surface of the tree as a whole is only 0.36%, the underlying

156 surface types evergreen coniferous forest, the mixed forest, the multiforest grassland mix and the

157 multigrass forestland mix will no longer be studied.

158 The MODerate-resolution Imaging Spectroradiometer (MODIS) is a sensor on board the

159 satellites TERRA and AQUA launched by the US Earth Observing System Program. The band of

160 the MODIS sensor covers the full spectrum from visible light to thermal infrared; thus, this sensor

161 can detect surface and atmospheric conditions, such as surface temperature, surface vegetation

162 cover, atmospheric precipitation, cloud top temperature, etc. The finest spatial resolution is 250 m.

163 The normalized vegetation index obtained by MODIS is the MYD13Q1 product, which provides a

164 global resolution of 250 m per 16 days. This study selects 73 data files for 2008, 2010 and 2012 in

165 Nagqu.

166 **2.2 Methodology**

167 **2.2.1 Method for calculating surface roughness by observation data**

168   Using the measured values of the average wind speed and turbulent flux of a single height

169 ultrasonic anemometer, the calculation scheme of surface roughness proposed by Chen et al.

170 (Chen et al., 1993) was selected and the dynamic variation in the surface roughness was obtained.

171   According to the Monin-Obukhov similarity theory (Monin et al., 1954), the wind profile

172 formula with the stratification stability correction function (Panosky et al, 1984) is as follows:

173
$$U(z) = \frac{u_*}{k}\left[\ln\frac{z-d}{Z_{0m}} - \psi_m(\zeta)\right] \qquad (1)$$

174
$$\psi_m(\zeta) = 2\ln(\frac{1+x}{2}) + \ln(\frac{1+x^2}{2}) - \tan^{-1}(x) + \frac{\pi}{2} \qquad \zeta < 0 \qquad (2)$$

175
$$\psi_m(\zeta) = -5\zeta \qquad \zeta > 0 \qquad (3)$$

176   where $u_* = \sqrt{-\overline{u'w'}}$; Z0m is the dynamic surface roughness length; z is the height of wind

177 observation; d is zero plane displacement, $d = 2/3h$(Stanhill, 1969), h is the vegetation height.

178 h takes 0 in winter, 0.020 in spring, 0.0450 in summer, and 0.030 in autumn in this study; U is the

179 average wind speed; k is the Karman constant, which is set to 0.40 (Högström,1996);

180 $L = -\dfrac{u_*^3}{(k\dfrac{g}{\theta})\overline{\theta'\omega'}}$ is the Monin-Obukhov length (Monin et al., 1954); $x = (1-16\zeta)^{1/4}$; and

181 $\zeta = (z-d)/L$ is the atmospheric stability parameter. Available from formula (1):

182

183
$$\ln\frac{z-d}{Z_{0m}} = \frac{kU}{u_*} + \psi_m(\zeta) \qquad (4)$$

184   Using equations (2)~(4), *Z0m* can be determined by fitting ζ and observing a single height

185 $\dfrac{kU}{u_*}$.

186 **2.2.2 Method for calculating surface roughness by satellite data**

187   For a fully covered uniform canopy, Brutsaert suggested that *Z0m* =0.13 hv (Brutsaert, 1982).

188 For a canopy with proportional coverage (partial coverage), Raupach (Raupach, 1994) indicated

189 that *Z0m* varies with the leaf area index (LAI). However, Pierce et al. (Pierce et al. 1992) pointed

190 out that for all kinds of biological groups, the leaf area index can be obtained from the NDVI and

191 the fractional cover of vegetation can be related to the NDVI. Asrar et al. (Asrar et al., 1992)

192 pointed out that a mutual relationship occurred among the LAI, NDVI and ground cover through

193 the study of physical models. Moran's study (Moran, et al., 1994) provides another method that

194 uses the function of the relationship between NDVI and Z_{0m} in the growing season of alfalfa.

195   Considering that the main underlying surface of the study area is grassland, this study selects

196 the Massman model (Massman et al, 1997, 1999) to calculate the Z0m in the Nagqu area of the

197 central Tibetan Plateau. The Massman model is calculated as follows:

198
$$\gamma = C_1 - C_2 \cdot exp(-C_3 \cdot C_d \cdot LAI) \qquad (5)$$

199
$$n_{ec} = \frac{C_d \cdot LAI}{2 \cdot \gamma^2} \qquad (6)$$

200
$$d_h = 1 - \frac{[1 - exp(-2 \cdot n_{ec})]}{2 \cdot n_{ec}} \qquad (7)$$

201
$$\frac{Z_{0m}}{h} = [1 - d_h] \cdot exp(-\frac{k}{\gamma}) \qquad (8)$$

202   where C_1=0.32, C_2=0.26, and C_3=15.1 are constants in the model and related to the surface

203 drag coefficient; LAI is the leaf area index; C_d=0.2 is the drag coefficient of the foliage elements;

204 n_{ec} is the wind speed profile coefficient of fluctuation in the vegetation canopy; and h is the

205 vegetation height. In many earlier studies, the high-altitude environment of the Tibetan Plateau

206 was correlated with a low temperature in the study area and shown to affect the height and

207 sparseness of the vegetation. Based on previous research, this study considers that the vegetation

208 height in northern Tibet is related to the normalized difference vegetation index (NDVI) and

209 altitude (Chen et al, 2013) and introduces the altitude correction factor on the original basis. The

210 following is the calculation formula:

211
$$H = h_{min} + (\frac{h_{max} - h_{min}}{NDVI_{max} - NDVI_{min}})(NDVI - NDVI_{min}) \qquad (9)$$

212
$$h = acf \cdot H \qquad (10)$$

213   where h_{min} and h_{max} are the minimum and maximum vegetation height observed at the

214 observation station, respectively, $NDVI_{max}$ and $NDVI_{min}$ are the maximum and minimum NDVI of

215 the observation station, respectively; H is based on the assumption that the vegetation height is

216 directly proportional to the NDVI; x is the altitude, which is obtained from ASTER's DEM

217 products; and acf is the altitude correction factor (Chen et al., 2013), which is used to characterize

218 the effect of elevation on the height of vegetation in northern Tibet. The acf parameter has the

219 following form:

220
$$acf = \begin{cases} 0.149, x > 4800 \\ 11.809 - 0.0024 \cdot x, 4300 < x < 4800 \\ 1.49, x < 4300 \end{cases} \quad (11)$$

221   The LAI used in this study is calculated by the NDVI of MODIS (Su,1996). The calculation

222 formula is as follows:

223
$$LAI = \left(\frac{NDVI * (1 + NDVI)}{1 - NDVI} \right)^{0.5} \quad (12)$$

224 **3 Results analysis**

225 **3.1 Variation characteristics of surface roughness based on measured data**

226   Figure 2 shows the temporal variation characteristics of the surface roughness of sites in

227 different years in the Nagqu area. The Z0m value has continued to increase since February to

228 reach a maximum in July and August. The results for the BJ and NPAM stations in 2012 show that

229 July has slightly larger ones than August, and the results for the NAMC station in 2010 and BJ

230 station in 2008 show that August has larger than July. After August, the Z0m value began to

231 decrease, and in December, the value was approximately the same as the value in January. In

232 general, the change in the Z0m degree of each station increases from spring to summer and

233 decreases month by month from summer to winter.

234 **Figure 2 about here**

235

236 **3.2 Spatiotemporal variation characteristics of surface roughness length**

237 **retrieved by MODIS data**

238   Figure 3 shows a plot of the surface roughness distribution of 200×200 km^2 around the BJ

239 site in 2008. In February, the *Z0m* decreased from January, which may have been due to snowfall,

240   temperature, etc., resulting in a small $Z0m$ that continued to decrease. Due to the rising

241   temperature and snow melting, $Z0m$ showed a slowly increasing trend from February to May and a

242   rapid increase from June to August. From June onwards, a large number of surface textures were

243   observed, indicating the complexity of the underlying surface. Whether the bulk surface or

244   vegetation had a more important impact on $Z0m$ is not clear. From May to August, obvious

245   changes in humidity, temperature and pressure caused by the plateau summer monsoon led to an

246   increase in the height and coverage of surface vegetation, and $Z0m$ peaked in August. In particular,

247   the change from May to June was very significant, which may have been related to the beginning

248   of the summer monsoon in June, the corresponding increase in precipitation, that accelerated the

249   growth of vegetation and the rapid rise of $Z0m$. In June, July, and August, continuous precipitation

250   and rising temperatures led to vigorous vegetation growth, although changes were not observed

251   after the vegetation reached maturity. The corresponding maximum value of $Z0m$ in the figure

252   remains unchanged, although due to high values in these three months, the area with high Z0m

253   values gradually expanded and reached the maximum range in August. From September to

254   December, as the plateau summer monsoon retreated, the temperature and humidity gradually

255   decreased. Compared with the plateau summer monsoon, the conditions were no longer suitable

256   for vegetation growth; thus, the contribution of vegetation to $Z0m$ was weakened, the surface

257   vegetation height gradually decreased, and $Z0m$ continued to decrease. Moreover, the area with

258   high $Z0m$ value also gradually decreased.

259   **Figure 3 about here**
260   **Figure 4 about here**

261   Figures 4 and 5 show the retrieved monthly surface roughness values in the BJ area in 2010

262   and 2012, respectively. Moreover, Z0m also showed a decrease from January to February in the

263   Nagqu area in 2010 and 2012. Starting in February, Z0m increased. Starting in June, Z0m

264   increased rapidly and reached the peak of the whole year in August. Subsequently, Z0m began to

265   decrease.

266   **Figure 5 about here**

267   Figures 3, 4, and 5 show that Z0m changes with the spatial and temporal scale. Z0m shows

268   different trends on different underlying surfaces. In November 2008, the Z0m in the Nagqu area

269   was small overall and generally as low as 1 cm. Historical data show that there is a large-scale

270   snowfall process in the Nagqu area at this time. Snowfall over the meadow causes the underlying

271   surface of the meadow to be homogeneous and flat, and after the snowfall falls, it is easy to form a

272   block with a scattered and discontinuous underlying surface. We subsequently determined that the

273   surface roughness of the area with ice and snow as the underlying surface is not more than 1 cm,

274   which is consistent with historical weather processes. Therefore, we think that snowfall caused the

275   Z_{0m} in November to be very small. From November to December, Z_{0m} showed a growing trend,

276   which may be due to temperature, unfrozen soil or other reasons that resulted in the melting of

277   snow, and then the surface roughness showed a growing trend (Zhou, 2017).

278   **3.3 Evaluation of satellite data retrieved results**

279   **Figure 6 about here**

280   The underlying surfaces of the three sites selected in this study are all alpine meadows. In

281   Figure 6, the NPAM site data calculation results are larger than the satellite data retrieved results

282   throughout the year. Only the values in September and October are very close, and the trends are

283   similar. The maximum value of the site data calculation is 5 cm and the satellite data retrieved

284   result is 4.5 cm. The maximum difference is in May at 1.7 cm. The NAMC station data calculation

285   results are very close to the satellite data retrieved results from April to November, although the

286   satellite data retrieved results are significantly larger than the site data calculation results in

287   January, March and December. The largest difference occurs in January, and the difference value

288   reaches 1.5 cm. In 2008, the calculation results of the BJ station data were larger than the satellite

289   data retrieved results throughout the year. The calculation results of the site data were very close to

290   the satellite data retrieved results from January to April and July to November, although a large

291   difference was observed in May, June and December, with the largest difference occurring in May

292   at 1.8 cm. In 2012, the BJ site data calculation results were consistent with the satellite data

293   retrieved results for the whole year, although the site data calculation results were larger than the

294   satellite data retrieved results from March to June, and the station data calculation results were

295   smaller than the satellite data retrieved at other times. As a result, the largest difference occurred

296   in June at 1.1 cm. Figure 6 shows that for the overall situation, the seasonal variation trend of the

297   site data calculation results is consistent with the satellite data retrieved results in January,

February, March, November and December. However, the site data calculation results from April to October are greater than the satellite data retrieved results. From Figure 6, the Z0m calculated from the site observation data is larger than that of the satellite data, which may be because of the average smoothing effect. From February to July, the single point Z0m value was significantly increased according to the independent method of determining the surface roughness, while the results obtained by using the satellite data did not increase significantly. The satellite results show that the values from January to May, November, and December are basically stable below 2 cm and only change from June to October, which is related to non-uniformity of underlying surface in Massman model. In general, the results calculated by the station are generally larger than those obtained by satellite retrieval.

Figure 7 about here

The Z0m scatter plot is shown in Figure 7. A significant positive correlation is observed between the satellite retrieval and the surface roughness calculated from the site data. The correlation coefficients between the observation result and the retrieved result are large except for at the NAMC station in 2010 in Figure 7(g). The average result of the underlying surface were consistent with the underlying surface results in different regions, further indicating that the satellite retrieved results are consistent with the site calculation results. However, the results of the NAMC site are different from those of the other sites. The correlation coefficient with the average results of the underlying surface is 0.83, and the correlation coefficient with the satellite retrieved results is 0.62. Because the NAMC Observation Station is closer to the lake (1 km), it is more affected by local microclimates, such as lake and land winds. The results in Figure 7 all passed the F test of P=0.05, which indicates that there is no significant difference between the site data calculation results and the satellite data retrieved results.

4 Variation characteristics of the surface roughness of different underlying surfaces

According to the vegetation dataset GLC2009 combined with actual local conditions, the 200×200 km^2 area of Nagqu was divided into 10 different underlying surfaces (Arino et al., 2010): mountain grassland, shrub meadow, mountain meadow, alpine grasslands, alpine meadows, sparse vegetation lap, urban land, bare land, water bodies, ice sheets and snow cover.

328 **Figure 8 about here**

329   The monthly variation in Z0m in different underlying surfaces in the Nagqu area is shown in

330 Figure 8, which indicates that 14 different underlying surfaces in the Nagqu area can be divided

331 into four categories. The first category is urban land, which accounts for 0.07% of the whole study

332 area. The Z0m of this type of underlying surface is greater than that of other types throughout the

333 year, and the change in Z0m is very large, which is probably due to the irregular changes in the

334 underground areas of the selected areas and the irregularities caused by human activities. The

335 second category is lush grassland, including shrub meadows, mountain grasslands, alpine

336 grasslands and mountain meadows, which account for 62.49% of the area. The variation curves of

337 Z0m of the four underlying surfaces are similar, and the Z0m of the urban land is only smaller

338 than that of other underlying surfaces. The third category is sparse grassland, including alpine

339 sparse vegetation, alpine meadows and bare land, and it accounts for 33.74% of the area. The Z0m

340 values of the three underlying surfaces are similar at a medium height. The Z0m of the bare soil is

341 at the lowest point of these underlying surface Z0m, and the Z0m of the alpine meadow is

342 relatively stable and less affected by the outside vegetation. The fourth category is ice and snow,

343 including ice surfaces and snow cover, and water bodies are two kinds of underlying surfaces,

344 accounting for 3.7% of the area. The Z0m of these three underlying surfaces presents another

345 phenomenon. The variation range of the whole year is relatively small, and the Z0m of these

346 underlying surfaces is also small. It is more than 1 cm in mid-June and less than 1 cm at other

347 times. Figure 8(d) shows the multiyear average seasonal variation in Z0m. The figure clearly

348 shows that the underlying surface can be divided into four categories due to the difference in

349 surface roughness. The change from January to May Z0m is very small, peaking from May to

350 August and then down to the previous January to May level in November and December. The

351 snowfall in November 2008 may have led to the low level of November in Figure 8(d). Table 2

352 shows that the winter albedo at the BJ station and NAMC station is higher than that in other

353 seasons, and the summer is the smallest. The surface albedo at both stations in November 2008

354 was significantly higher than that in November of the other two years. In fact, the surface

355 roughness in November should be higher than that in December in former years.

356 **Table 2 about here**

357 Figure 8 also shows that in the Nagqu area, except for the area of the fourth type of

358 underlying surface, the Z0m change in other areas decreases from January to February and begins

359 to increase after February, reaching a peak in August and then starting to decrease. However,

360 Figure 6 clearly shows that there are several stages in which Z0m changes significantly, in early

361 April, mid-May, early July, late August, and late September. The change at the end of August was

362 the most obvious. At each of the underlying surfaces Z0m changes by more than 2 cm on average.

363 The extent of the change in late September was also large, with an average change of more than

364 1.5 cm. Moreover, the change in early July was special because the change resulted in a significant

365 increase in the Z0m of water bodies and ice.

366 Certain factors, such as cloud cover in May, August, and November of 2008; August and

367 September of 2010; and April and July of 2012, caused significant changes in the overall Z0m,

368 which resulted in two very significant changes in the three-year average for August and November.

369 In November, the change was caused by snowfall based on other meteorological data. In August

370 2008 and 2010, the changes were caused by precipitation based on an analysis of the sudden

371 increase in the Z0m of the water body and ice and snow surface. Combined with several changes

372 in Z0m, precipitation, snowfall, and snow accumulation will make the underlying surface more

373 uniform and flatter, which will lead to relative reductions in Z0m.

374 # 5 Simulation and evaluation the impact of surface roughness on

375 # turbulent fluxes using Noah-MP model

376 ## 5.1 Model setup

377 According to the surface roughness variation characteristics retrieved from

378 satellite data, the underlying surface of Nagqu area can be divided into four types.

379 They are urban, lush grass, sparse grass, and ice and snow. Among them, urban

380 accounts for 0.07%, its Z0m up to 9 cm, lush grassland accounts for 62.49% of the

381 area, its Z0m can reach up to 6cm, sparse grassland up to 33.74%, its Z0m can reach

382 up to about 4cm, ice and snow accounts for 3.7% of the area, and Z0m does not

383   exceed 1cm. These results are substituted into Noah- MP to replace the original

384   parameter design numerical simulation experiment. The model after replacing the

385   surface roughness is set as a sensitivity experiment, and the original model is set as a

386   control experiment. The selection of other parameterization schemes suitable for

387   numerical simulation in Nagqu area is shown in Table 3. The simulation time is from

388   July 1 to 31, 2008, and the spin-up time is 9 days. The forcing field dataset is a

389   Chinese meteorological forcing dataset (He et al., 2020) jointly developed by the

390   Tibetan Plateau Data Assimilation and Modelling Centre and the Institute of Tibetan

391   Plateau Research of the Chinese Academy of Sciences (ITPCAS).

392   **5.2 Evaluation of the simulated single point heat flux**

393   Figure 9(a) shows that the sensible heat flux simulated by the sensitivity

394   experiment is closer to the measured value than the control experiment at BJ site. In

395   the daytime, the results of sensitivity experiment were in general smaller than those of

396   the control experiment. At night, the results of the two models were close to each

397   other before July 21, and the sensitivity experiment results were significantly

398   improved after July 21. Figure 9(b) shows that the sensitivity experiment results are

399   basically consistent with the control experiment results at BJ site, which are

400   maintained at about 0 W/m^2, and there is no improvement at night. Before July 19, the

401   latent hear fluxes for the two experiments remained at about 200 W/m^2, which was

402   less than the observed latent heat flux, and the simulated maximum value of the

403   sensitivity experiment was greater than that of the control experiment. After July 19,

404   the two experiments simulation results began to increase and reached about 400 W/m^2

405   consistent with the observed latent heat flux, indicating that the simulation effect was

406   improved to some extent. Similarly, it can be found from the maximum value that the

407   sensitivity experiment results were slightly greater than the control experiment results.

408   The simulated values of sensible heat fluxes at NAMC and NPAM sites (Fig.9 c, e)

409   are significantly larger than the observation results, but the sensitivity experiment

410   results are better than the control experiments, while latent heat flux in the sensitivity

411 experiment are greater than that in the control experiment and are close to the

412 observation results at NPAM site (Fig. 9 f). It also shows that improving the accuracy

413 of surface roughness can improve the simulation effect of latent heat flux.

Figure 9 about here

5.3 Evaluation of regional heat flux simulation results

416   In order to compare the changes of sensible heat flux and latent heat flux before

417 and after improvement, the sensitivity simulations are used to subtract the control

418 model simulation results. By subtracting the sensible heat flux of control from

419 sensitivity experiment, the results are shown in the figure 10. It can also be seen from

420 the figure 10 (a) that the difference of sensible heat flux is basically negative in the

421 daytime, indicating that the sensible heat flux after improvement is smaller than that

422 before improvement. The above results show that the modified surface roughness can

423 improve the simulation effect of sensible heat flux in daytime. The results in the

424 figure 10 (c) are basically positive in the daytime, indicating that the latent heat flux

425 after improvement is larger than that before improvement, about $15W/m^2$. The above

426 results show that the model simulation results are generally less than the actual

427 observation results, so it can be considered that the improvement of surface roughness

428 in the daytime can improve the simulation of heat fluxes. Figure 10 also shows that

429 the improvement of night time latent heat flux is not significant, which is basically

430 maintained at $0W/m^2$.

Figure 10 about here

6 Conclusions and discussion

433   Through the calculation and analysis of the surface roughness of the Nagqu area in the

434 central Tibetan Plateau and comparing the retrieved satellite data with the calculation results of the

435 observational data, the attained main conclusions are as follows.

436   (1) The retrieved results of the satellite data are basically consistent with the calculated

437 results of the measured data. Both results indicate that the surface roughness continued to increase

438 from February to August, began to decrease after reaching a peak in August and reached the

439 lowest value in February of the following year. A strong connection is observed between the

440 monthly variation in surface roughness and the changes in meteorological elements brought by the

441 plateau summer monsoon. Among them, the satellite surface retrieval results in a slow increase in

442 surface roughness from February to May.

443   (2) Through the characteristics of surface roughness variation retrieved by satellite data, the

444 underlying surface can be divided into four categories according to the surface roughness (from

445 large to small): urban, lush grassland, sparse grassland and ice and snow. Among them, lush

446 grassland accounts for 62.49%, and the Z_{0m} can reach 6 cm; sparse grassland accounts for 33.74%,

447 and the Z_{0m} can reach up to 4 cm; and ice and snow account for 3.7%, and the Z_{0m} does not exceed

448 1 cm.

449   (3) Comparing satellite retrieved results and measured data shows that the results are

450 positively correlated and the satellite retrieved results are better fit with the measured results. Due

451 to the average sliding effect of the retrieved data, the satellite retrieved data are smaller than the

452 measured results. This method can be used to calculate the surface roughness results for a region

453 and provide a true value for the model for simulation.

454   (4) The accuracy of ground-air flux simulation can be improved after adjusting the surface

455 roughness in Nagqu area. After replacing the model surface roughness, the sensible heat flux has

456 been improved by 20 W/m^2 during the daytime. The improvement for simulation of sensible heat

457 flux is poor at night, about 0.15W/m^2. The improvement of latent heat flux is not obvious, and

458 there is an improvement within 15W/m^2 during the daytime.

459   This study uses remote sensing images and an aerodynamic roughness remote sensing

460 retrieved model to estimate the spatial scale of aerodynamic roughness conditions in northern

461 Tibet, and this method will provide parameter and parameterization scheme improvements for

462 model simulations to study the spatial distribution of the surface flux in the Tibetan Plateau. Air

463 thermodynamics surface roughness (Z_{0h}) is affected by shortwave and longwave radiation (the

464 latter for deriving surface temperature), air temperature, wind speed, precipitation or snowfall. The

465 relationship between air thermodynamics surface roughness and these other variables and how to

466 parameterize them in Massman model will be studied in the future.

Acknowledgements:

This work was financially supported by the Second Tibetan Plateau Scientific Expedition and Research (STEP) program (Grant No. 2019QZKK0103), the National Natural Science Foundation of China (Grant No. 41675106,41805009), National key research and development program of China (2017YFC1505702) and Scientific Research Project of Chengdu University of Information Technology (KYTZ201721).

References:

Arino O, Ramos J, Kalogirou V, et al."Glob Cover 2009"[R].Edinburgh, UK:Proceedings of the living planet Symposium, 2010.

Asrar , G ., Myneni , R.B.and Chaudhury , B.J., 1992, Spatial heterogeneity in vegetation canopies and remote sensing of observed photosynthetically active radiation:a modeling study , Ren.Sens.Env ., 41, 85～103.

Brutsaert , W.A ., 1982, Evaporation into the Atmosphere , Dordrecht in Holland , D .Reidel Publishing Company,113 ～ 121.

Chu D., Basabta S., Wang W., et al, 2010. Land Cover Mapping in the Tibet Plateau Using MODIS Imagery[J]. Resources Science, 32(11): 2152-2159. (in Chinese with English abstract)

Chen, J., Wang, J., Mitsuaki, H., 1993. An independent method to determine the surface roughness length. Chin. J. Atmos. Sci. 1993, 17, 21–26. (in Chinese with English abstract)

Chen Q., L. Jia, R. Hutjes, M. Menenti, 2015, Estimation of Aerodynamic Roughness Length over Oasis in the Heihe River Basin by Utilizing Remote Sensing and Ground Data, Remote Sensing, 2015, 7(4), 3690-3709; doi:10.3390/rs70403690.

Chen X., et al, 2013. An improvement of roughness height parameterization of the Surface Energy Balance System (SEBS) over the Tibetan Plateau[J]. Journal of Applied Meteorology and Climatology, 52(3): 607-622.

Guan X., Huang J., et al, 2009. Variability of soil moisture and its relationship with surface albedo and soil thermal parameters over the Loess Plateau[J]. Advances in Atmospheric Sciences, 26(4): 692-700, doi: 10.1007/s00376-009-8198-0.

He, J., Yang, K., et al., 2020. The first high-resolution meteorological forcing dataset for land process studies over China. Scientific Data, 7, 25, https://doi.org/10.1038/s41597-020-0369-y.

Högström U., 1996 'Review of Some Characteristics of the Atmospheric Surface Layer' Boundary-Layer Meteorol 78 215–246 10.1007/BF00120937

Irannejad P, Shao Y P, 1998. Description and validation of the atmosphere-land-surface interaction scheme(ALSIS)with HAPEX and Cabauw data[J]. Global Planet Change,   19(1): 87-114.

Jane Q., 2008. The third pole[J]. Nature, 454(24): 393-396.

Jia L., Wang J., Hu Z., 2000. The Characteristics of Roughness Length for Heat and Its Influence on Determination of Sensible Heat Flux in Arid Zone[J]. Plateau Meteorology,   19(04): 495-503. (in Chinese with English abstract)

Li F., Li S., Chen T., 2004. A Study on Develpoment of the Tibetan North Grasslands Tourism Stockbreeding in Naqv Tibet[J]. Sichuan Caoyuan,   109(12): 38-42. (in Chinese with English abstract)

Li J., Hong Z., Sun S., 2000. An Observational Experiment on the Atmospheric Boundary Layer in Gerze Area of the Tibetan Plateau[J]. Chinese Journal of Atmospheric Sciences, 24(03): 301-312. (in Chinese with English abstract)

Li L., Chen X., Wang Z., et al, 2010. Climate Change and Its Regional Differences over the Tibetan Plateau[J]. Advances in Climate Change Research,   6(03): 181-186. (in Chinese with English abstract)

Liu J., Zhou M., Hu Y., 2007. Discussion on the Terrain Aerodynamic Roughness[J]. Ecology and Environment,   16(06): 1829-1836. (in Chinese with English abstract)

Luo S., Lü S., Yu Z. (2009) Development and validation of the frozen soil parameterization scheme in Common Land Model. Cold Reg Sci Technol 55:130–140

Ma Y., Tsukamoto O, Wang J., et al, 2002. Analysis of aerodynamic and thermodynamic parameters on the grassy marshland surface of Tibetan Plateau[J]. Progress in Natural Science, 12(1): 36-40.

Ma Y., Wang J., et al, 2002. Analysis of Aerodynamic and Thermodynamic Parameters on the Grassy Marshland Surface of Tibetan Plateau[J]. Peogress in Natural Science, 12(01): 36-40. (in

Chinese with English abstract)

Ma Y., Yao T., Wang J., et al, 2006. The Study on the Land Surface Heat Fluxes over Heterogeneous Landscape of the Tibetan Plateau[J]. Advances in Earth Science, 21(12): 1215-1223. (in Chinese with English abstract)

Massman W., 1997. An analytical one-dimensional model of momentum transfer by vegetation of arbitrary structure[J]. Boundary-Layer Meteorology, 83(3): 407-421.

Massman W., 1999. An analytical one-dimensional second-order closure model of turbulence statistics and the Lagrangian time scale within and above plant canopies of arbitrary structure[J]. Boundary-Layer Meteorology, 91(1): 81-107.

Monin A., Obukhov A., 1954. Basic laws of turbulent mixing in the atmosphere near the ground[J]. Tr Akad Nauk SSSR Geofiz Inst, 24(15): 163-187.

Moran, M .S ., Clarke , T .H., Inone, Y.et al., 1994, Estimating crop water deficit using the relation between surface-air temperature and spectral vegetation index, Rem .Sens. of Env ., 49 , 246 ～ 263.

Panosky H., Dutton J., 1984. Atmospheric Turbulence: Models and Methods for Engineering Applications[M]. New York: John Wiley, 1-399.

Pierce , L.L., Walker, J., Downling , T .I.et al., 1992, Ecological change in the Murry -Darling Basin-III :A simulation of regional hydrological changes , Journal of Applied Ecology , 30, 283～ 294.

Raupach, M .R., 1994, Simplified expressions for vegetation roughness leng h and zero-plane displacement as functions of canopy height and area index , Boundary -Layer Meteor ., 71, 211-216.

Shao Y., 2000. Phtsics and Modeling of Wind Erosion[M]. London: Kluwer Academic Publishers, 1-452.

Smirnova T., Brown J., Benjamin S., Kenyon J. (2016) Modifications to the rapid update cycle land surface model (RUC LSM) available in the weather research and forecasting (WRF) model. Mon Weather Rev 144(5):1851–1865

Stanhill G., 1969. A simple instrument for the field measurement of turbulent diffusion flux. J

551   Appl Meteorol 8:509–513

552   Stull B R, 1991. An Introduction to Boundary Layer Meteorology[M]. Beijing: China

553   Meteorological Press, 1-737.

554   Su, Z., 1996. Remote Sensing Applied to Hydrology: The Sauer River Basin Study.

555   RuhrUniversität Bochum, Lehrstuhl für Hydrologie, Wasserwirtschaft und Umwelttechnik.

556   Tao S., Chen, L., Xu X., et al, 1998. Progresses of the Theoretical Study in the Second Tibetan

557   Plateau Experiment of Atmospheric Sciences (PartI)[M]. Beijing: China Meteorological Press,

558   1-348.

559   Wu G., Mao J., Duan, A., et al., 2004. Recent progress in the study on the impact of Tibetan

560   Plateau on Asian summer climate[J]. Acta Meteorologica Sinica, 62(5): 528-540. (in Chinese with

561   English abstract)

562   Wu G., Zhang Y., 1998. Tibetan Plateau forcing and timing of the Mon-soon onset over south Asia

563   and the south China sea[J]. Monthly Weather Review, 4(126): 913-927.

564   Wu G., Zhang Y., 1999. Thermal and Mechanical Forcing of the Tibetan Plateau and Asian

565   Monsoon Onset.Part Ⅱ:Timing of the Onset[J]. Chinese Journal of Atmospheric Sciences,

566   23(01): 52-62. (in Chinese with English abstract)

567   Wu G., Liu Y., Liu X., et al. 2005. How the heating over the Tibetan Plateau affects the Asian

568   climate in summer[J]. Chinese Journal of Atmospheric Sciences, 29(1): 47-56. (in Chinese with

569   English abstract)

570   Wu X., Ma W., Ma Y., 2013. Observation and Simulation Analyses on Characteristics of Land

571   Surface Heat Flux in Noethern TibetanPlateau in Summer[J]. Plateau Meteorology, 32(05):

572   1246-1252. (in Chinese with English abstract)

573   Xie Z., Hu Z., Liu H., Sun G., et al., 2017 Evaluation of the Surface Energy Exchange Simulations

574   of Land Surface Model CLM4.5 in Alpine Meadow over the Qinghai-Xizang Plateau. Plateau

575   Meteorology, 36(1): 1-12. (in Chinese with English abstract)

576   Xu L., Liu H., Xu X., et al. 2018, Applicability of WRF model to the simulation of atmospheric

577   boundary layer in Nagqu area of Tibetan Plateau[J]. Acta Meteorologica Sinica, 2018(6):955-967.

578   (in Chinese with English abstract)

579   Yang M., Yao T., 1998. A Review of the Study on the Impact of Snow Cover in the Tibetan

580   Plateau on Asian Monsoon[J]. Journal of Glaciology and Geocrylolgy,   20(2): 90-95. (in Chinese

581   with English abstract)

582   Ye D., Wu G., 1998. The role of heat source of the Tibetan Plateau in the general circulation[J].

583   Meteorological and Atmospheric Physics, 67(1): 181-198.

584   Zhang G., Zhou G., Chen F. 2017, Analysis of Parameter Sensitivity on Surface Heat Exchange in

585   the Noah Land Surface Model at a Temperate Desert Steppe Site in China[J]. Acta Meteorologica

586   Sinica. (6).1167-1182.doi:10.1007/s13351-017-7050-1.

587   Zhang Q., Lv S., 2003. The Determination of Roughness Length over City Surface[J]. Plateau

588   Meteorology,   22(01): 24-32. (in Chinese with English abstract)

589   Zhang Y., Wu G., 1998. Diasnostic Investigations of Mechanism of Onset of Asian Summer

590   Monsoon and Abrupt Seasonal Transitions Over Northern Hemisphere PartI[J].   Acta

591   Meteorologica Sinica,   56(5): 2-17. (in Chinese with English abstract)

592   Zhou X., Zhao P., Chen J., et al, 2009. Impacts of Thermodynamic Processes over the Tibetan

593   Plateau on the Northern Hemispheric Climate[J]. Sci China Ser D-Earth Sci,   39(11): 1473-1486.

594   (in Chinese with English abstract)

595   Zhou, Y., Ju, W., Sun, X., Wen, X., Guan, D. 2012 Significant decrease of uncertainties in sensible

596   heat flux simulation using temporally variable aerodynamic roughness in two typical forest

597   ecosystems of China. J. Appl. Meteorol. Climatol. 2012, 51, 1099–1110.

598   Zhou Y., Xu W., Bai A., et al, 2017. Dynamic Snow-melting Process and its Relationship with Air

599   Temperature in Tuotuohe, TibetanPlateau[J]. Plateau Meteorology, 36(1): 24-32. (in Chinese with

600   English abstract)

601

602   Figure captions

603   Fig. 1 Location of sites and the land cover on the northern Tibetan Plateau. The black solid circle

604   '●' indicates the location of the sites

605   Fig. 2 Surface roughness length of different sites on the northern Tibetan Plateau

606   Fig. 3 Surface roughness length on the northern Tibetan Plateau in 2008

607   Fig. 4 Surface roughness length on the northern Tibetan Plateau in 2010

608   Fig. 5 Surface roughness length on the northern Tibetan Plateau in 2012

609   Fig. 6 Comparison of the surface roughness length by site observations and satellite remote sense

610   retrieved data

611   Fig. 7 Scatter plots of the retrieved and calculated surface roughness lengths at four sites

612   Fig. 8 Curve of the surface roughness length for different underlying surfaces

613   Fig.9 Comparison of simulated and observed sensible heat flux (a, c, e) and latent heat flux (b, d, f)

614   at BJ, NAMC, NPAM sites respectively.

615   Fig. 10 The difference of the control and sensitivity experiments simulated regional sensible heat

616   flux (a) 12:00, (b) 00:00 and latent heat flux (c) 12:00, (d) 00:00

617

618   Tables

619   Table 1. Legend of the land cover map on the northern Tibetan Plateau

Value	Colour	Land Cover Types	Percent (%)	
11		Mountain grassland	5.79	620
14		Shrub meadow	3.25	621
20		Mountain meadow	8.26	622
30		Alpine grassland	45.16	623
70		Needle-leaved evergreen forest	0.23	624
100		Mixed forest	0.03	625
110		Mixed forestland and grassland	0.06	

Value	Colour	Land Cover Types	Percent (%)
120		Mixed grassland and	0.04
140		Alpine meadow	28.28
150		Alpine sparse vegetation	0.29
190		Urban areas	0.07
200		Bare areas	4.90
210		Water bodies	2.57
220		Permanent snow and ice	1.07

626   Table 2 the observed albedo of the sites (BJ and NAMC) on the northern Tibetan
627   Plateau

Site	year	Jan.	Feb.	Mar.	Apr.	May.	Jun.	Jul.	Aug.	Sep.	Oct.	Nov.	Dec.
BJ	2008	0.13	0.17	0.14	0.13	0.12	0.10	0.09	0.09	0.09	0.16	**0.32**	0.16
	2009	0.30	0.26	0.30	0.25	0.26	0.21	0.19	0.19	0.21	0.26	0.24	0.26
	2010	0.26	0.30	0.31	0.30	0.34	0.22	0.19	0.18	0.18	0.35	0.26	0.27
NAMC	2008	0.28	0.28	0.31	0.28	0.25	0.21	0.17	0.18	0.18	0.30	**0.89**	0.28
	2009	0.35	0.32	0.28	0.24	0.26	0.22	0.19	0.17	0.22	0.24	0.31	0.27
	2010	0.45	0.23	0.25	0.24	0.29	0.22	0.20	0.17	0.18	0.40	0.35	0.24

628
629
630
631
632
633

634

635
Table 3 The selected other schemes in Noah-MP

Options for different schemes	Name of the option
dynamic vegetation	Use table LAI; use FVEG=SHDFAC from input
canopy stomatal resistance	Ball-Berry's method
soil moisture factor for stomatal resistance	Noah's method
runoff and groundwater	TOPMODEL with groundwater
surface layer drag coeff	Monin-Obukhov's method
supercooled liquid water	No iteration
frozen soil permeability	Nonlinear effects, less permeable
radiation transfer	Two-stream applied to grid-cell
ground snow surface albedo	Classic method
partitioning precipitation into rainfall & snowfall	Jordan's method
lower boundary condition of soil temperature	TBOT at ZBOT (8m) read from a file
snow/soil temperature time scheme	full implicit (original Noah); temperature top boundary condition

636

637
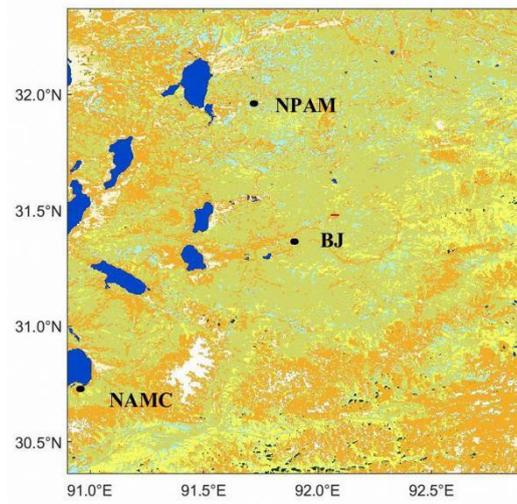
638

639   Fig. 1 Location of the sites and the land cover on the northern Tibetan Plateau. The black solid

640   circle '●' indicates the location of the sites.

641
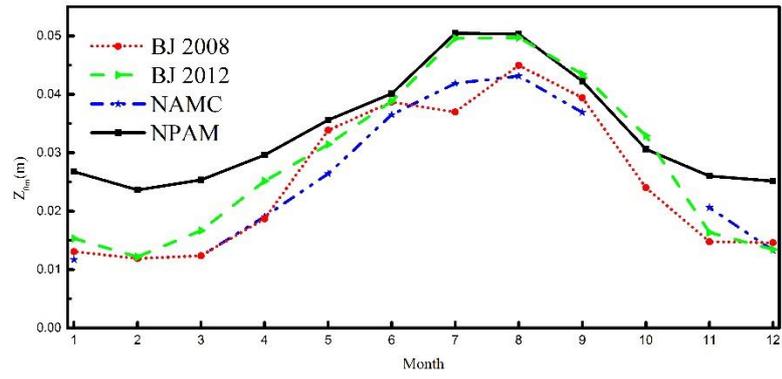
642

643   Fig. 2 Surface roughness length of different sites on the northern Tibetan Plateau. NPAM, NAMC,

644   BJ2008, BJ2012 refers to the annual variation of the roughness lengths in 2012 at NPAM site, in

645   2010 at NAMC site, in 2008 and in 2012 at BJ site respectively.

646
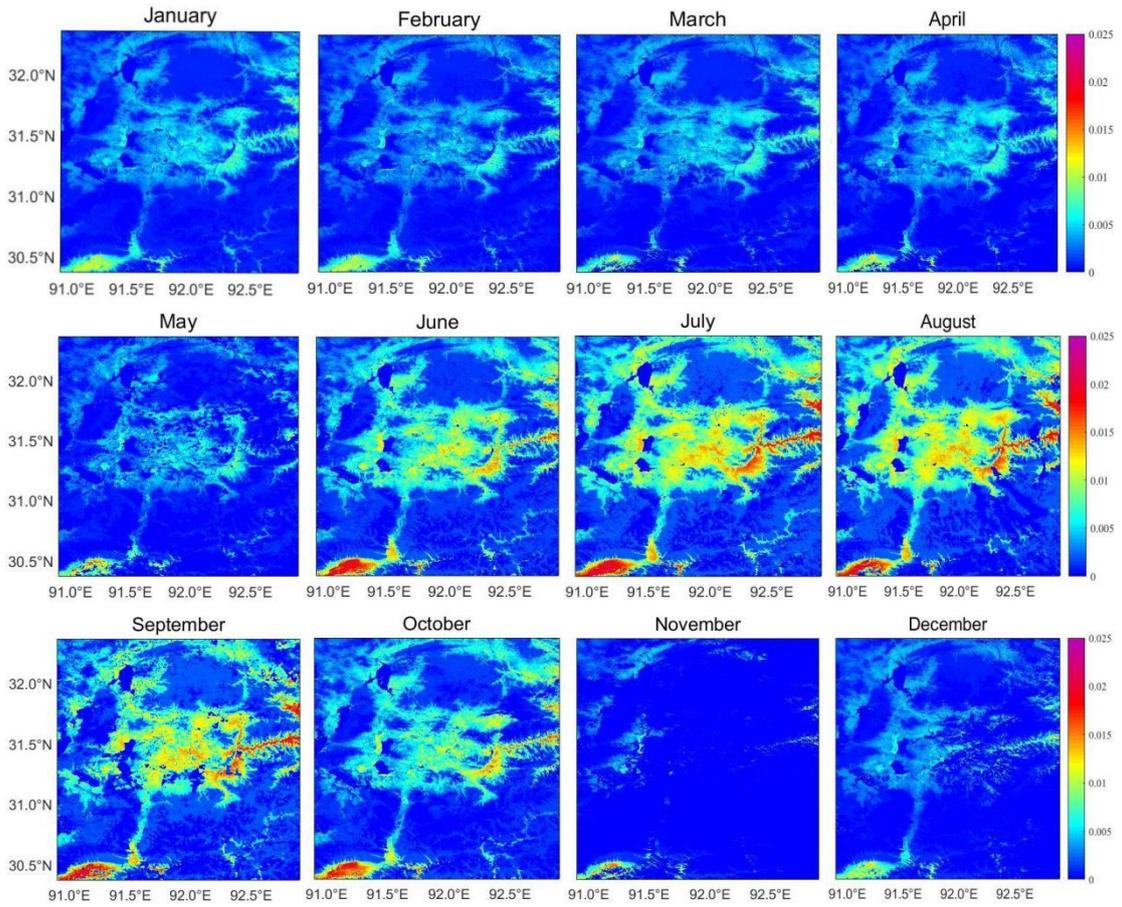
647

648

649

650   Fig. 3 Surface roughness length on the northern Tibetan Plateau in 2008

651

652

653

654

655
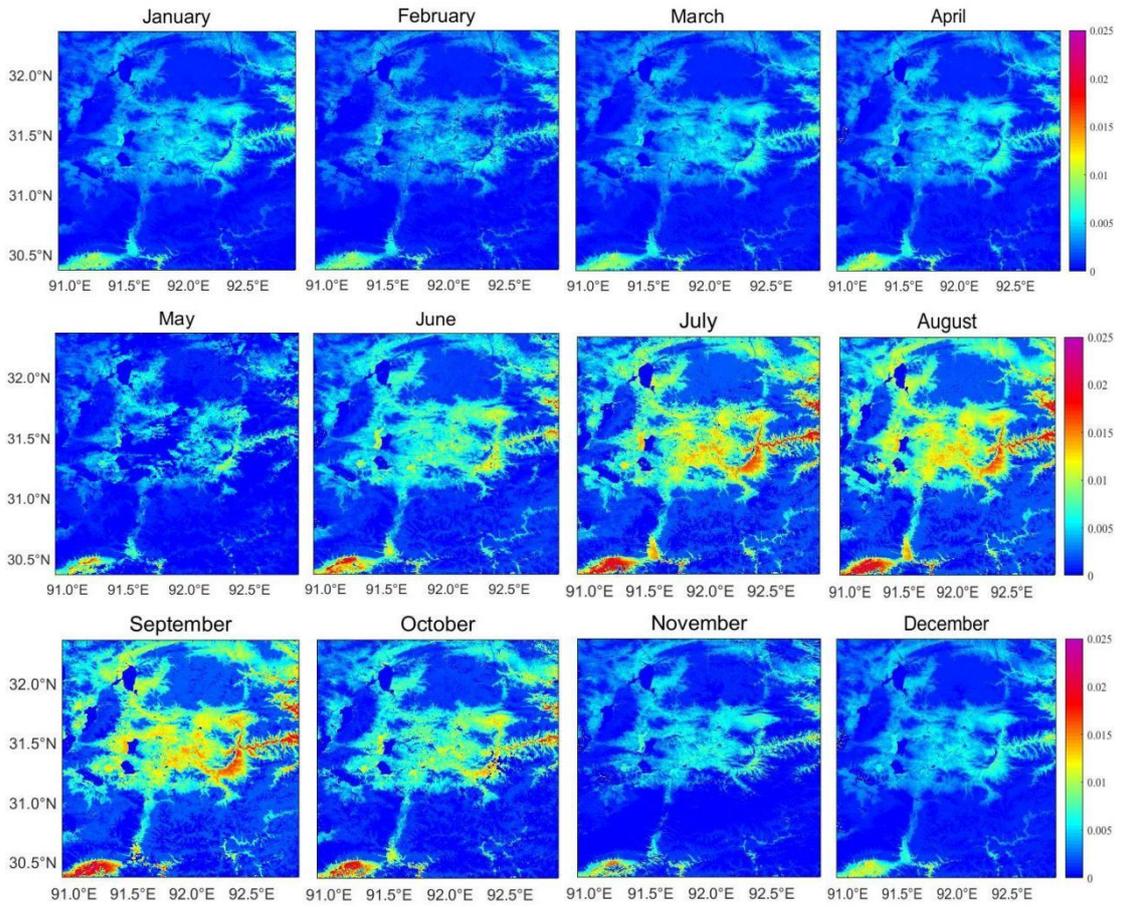
Fig. 4 Surface roughness length on the northern Tibetan Plateau in 2010

656

657

658

659

660

661
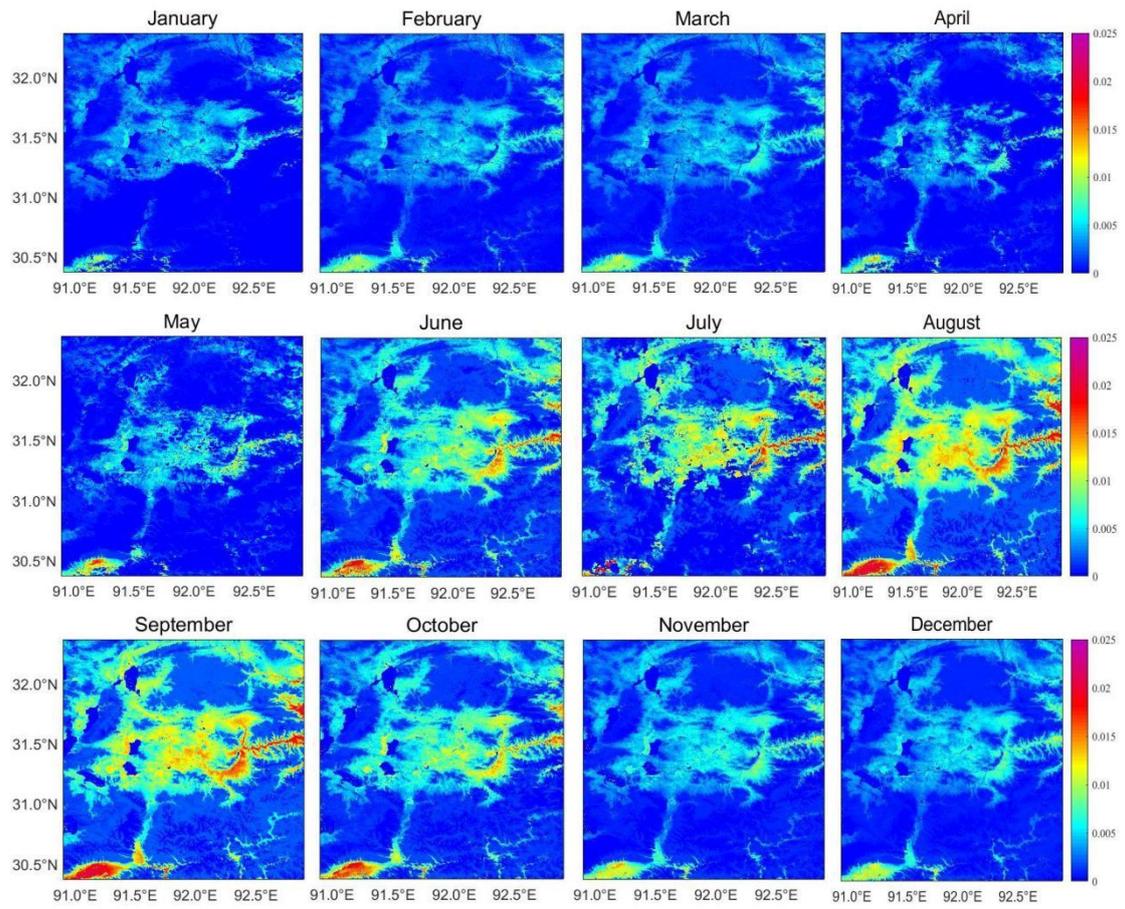
Fig. 5 Surface roughness length on the northern Tibetan Plateau in 2012

662

663
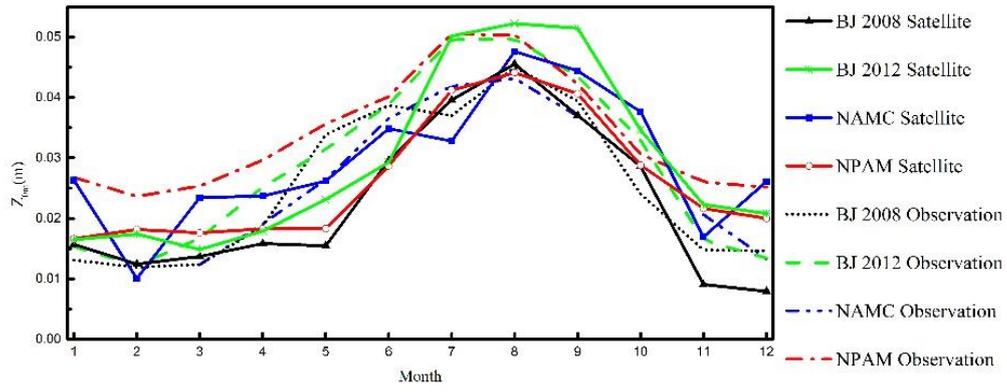
664

665   Fig. 6 Comparison of the surface roughness length by site observations and satellite remote sense

666   retrieved data

667
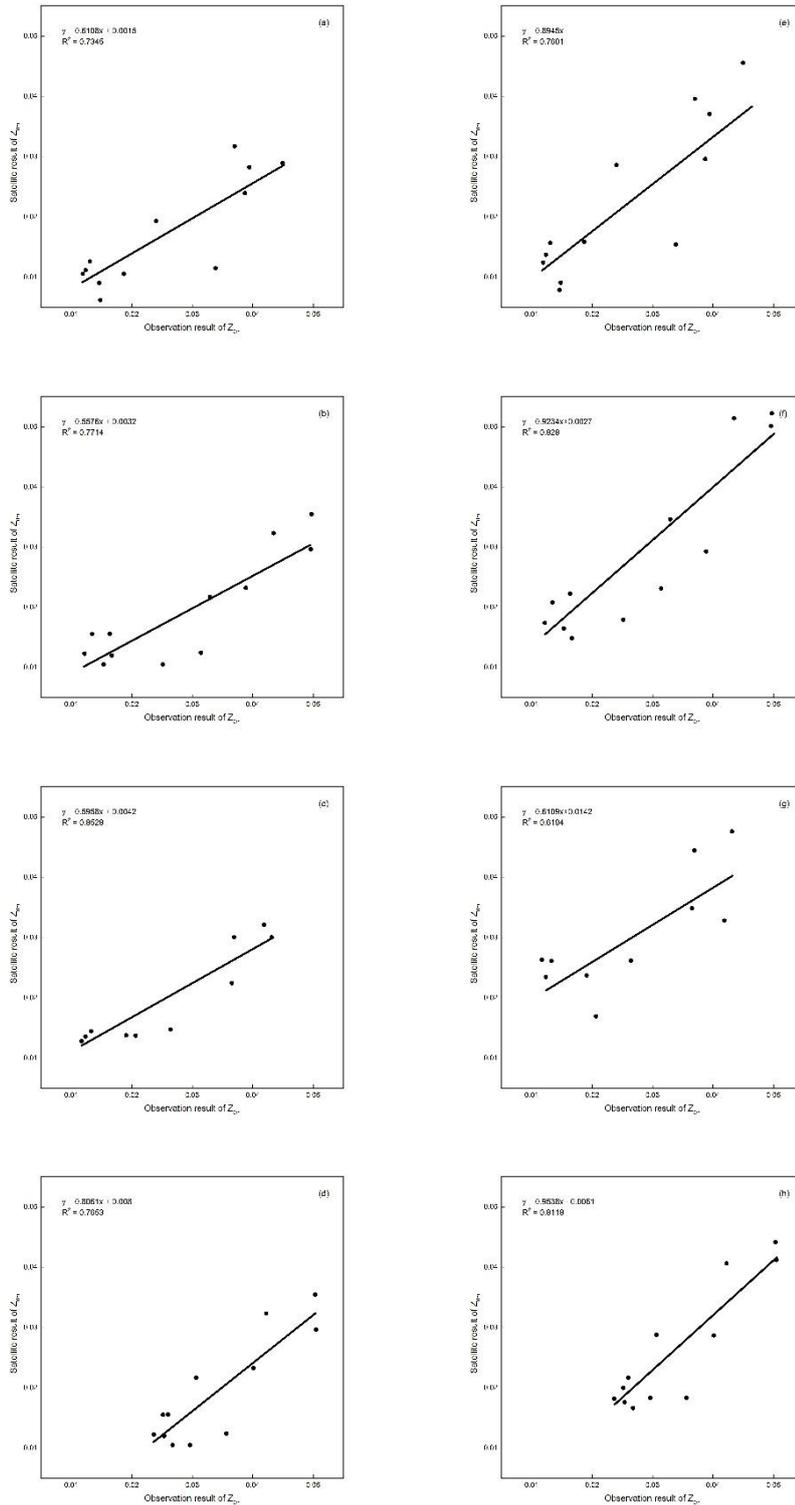
668   Fig. 7 Scatter plots of the retrieved and calculated surface roughness lengths at four sites

669   (a-d: scatter plot of the observation results and the average result of the underlying surface; e-h:

670   scatter plot of the observation and retrieved results; a, e: BJ station in 2008; b, f: BJ station in

671   2012; c, g: NAMC station in 2010; and d, h: NPAM station in 2012)
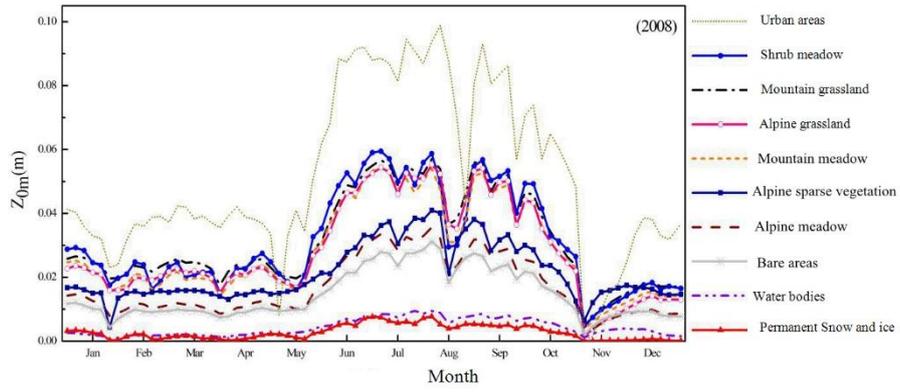
672
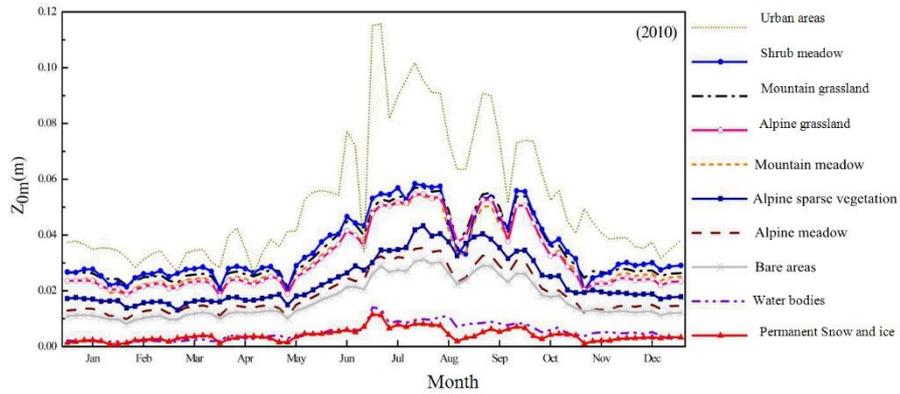
673
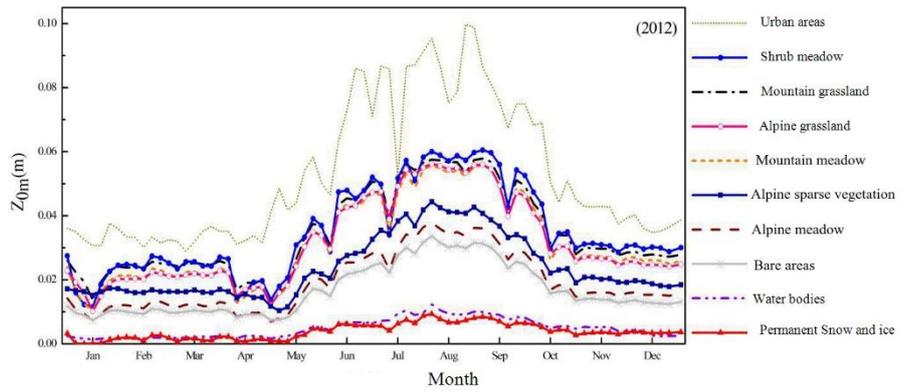
674
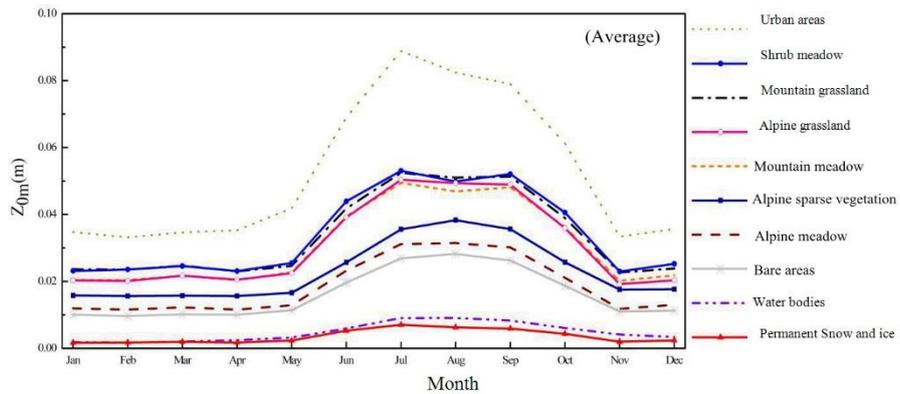
675

676   Fig. 8 Curve of the surface roughness length for different underlying surfaces

677
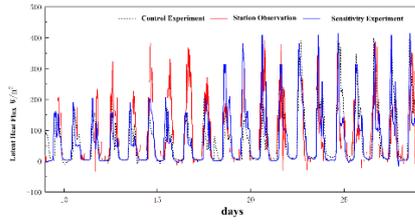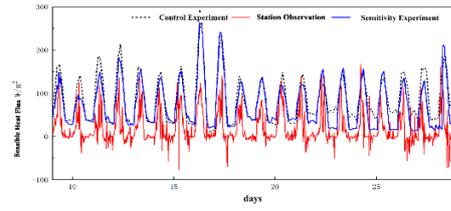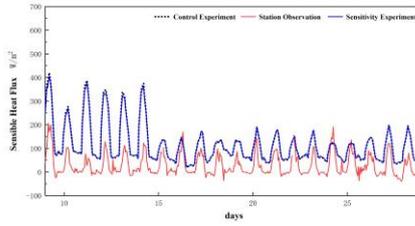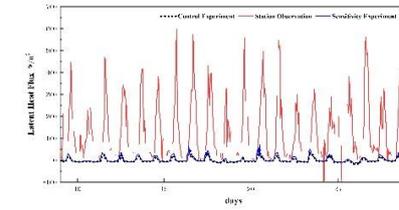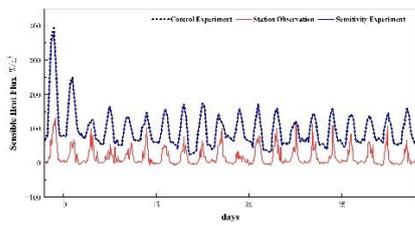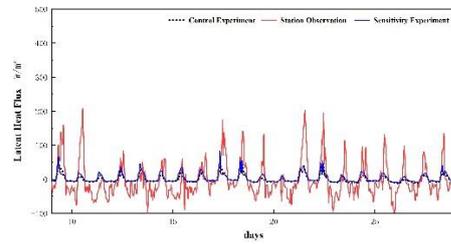
678

679   Figure 9 Comparison of simulated and observed sensible heat flux (a, c, e) and latent heat

680   flux (b, d, f) at BJ, NAMC, NPAM sites respectively.

681
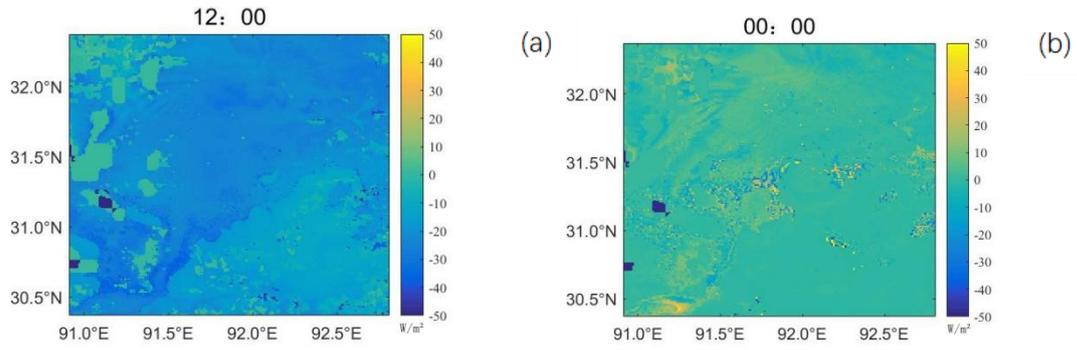
682

683
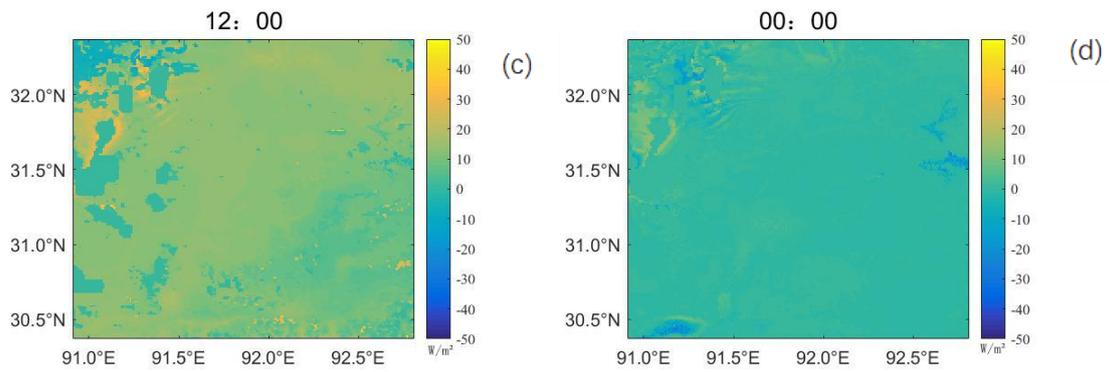
684

685 Figure 10 The difference of the control and sensitivity experiments simulated
686 regional sensible heat flux (a) 12:00, (b) 00:00 and latent heat flux (c) 12:00, (d)
687 00:00

688

689

690